Type II hot corrosion of the polycrystalline nickelbased superalloy AD730 in presence of Na 2 SO 4 and Na2SO4 -MgSO4 deposits

D. Diomande, Pierre-Jean Panteix, S. Migot, J. Ghanbaja, L. Aranda, C. Clément, M. Vilasi, S. Mathieu

Type II hot corrosion of the polycrystalline nickel-based superalloy AD730 in presence of Na_2SO_4 and Na_2SO_4-$MgSO_4$ deposits

D. Diomande, P-J. Panteix, S. Migot, J. Ghanbaja, L. Aranda, C. Clément, M. Vilasi, S. Mathieu*

Université de Lorraine, CNRS, IJL, Nancy, France

djeneba.diomande@cea.com; pierre-jean.panteix@univ-lorraine.fr; sylvie.migot@univ-lorraine.fr; jaafar.ghanbaja@univ-lorraine.fr; lionel.aranda@univ-lorraine.fr; christine.clement@univ-lorraine.fr; michel.vilasi@univ-lorraine.fr; stephane.mathieu@univ-lorraine.fr

*corresponding author

Keywords. Molten salts, Hot corrosion, Nickel-based superalloys, HR-TEM, sulfation

Abstract

The type II corrosion resistance of AD730 was studied at 650 °C and 700 °C in air + 400 ppm SO_2 (g), in the presence of Na_2SO_4 and Na_2SO_4-$MgSO_4$ deposits. At 650°C, the pit-like attacks were of similar depth for both salts and less severe than those observed at 700°C. Although the sulfate mixture (Na_2SO_4-$MgSO_4$) was liquid at 700°C from the beginning of the exposure, it proved to be less aggressive than Na_2SO_4. Wavelength dispersive spectrometry characterization of the pits revealed the systematic stratification of the oxides from the alloy-corrosion products interface toward the corrosion products-gas interface across the pit corrosion products, i.e. the establishment of a gradient of oxygen ions activity. High resolution transmission electron microscopy highlighted a high level of porosity, sulfur enrichment as well as the presence of the WS_2 sulfide, with an anisotropic bidimensional structure, located at the alloy-oxide interface. Sulfation tests carried out on nickel oxide and cobalt oxide in the presence of Na_2SO_4 and Na_2SO_4-$MgSO_4$ showed little sulfation with the magnesium-containing salt, thus demonstrating how $MgSO_4$ contributes to limit the corrosion at 700°C. The results demonstrated that the severe hot corrosion attacks are not only related to the formation of a liquid phase, but also to its chemical composition.

1. INTRODUCTION

Enhancing aircraft gas turbine (GT) overall efficiency supposes the increase of their operating temperature. After decades of materials development, ever more efficient, the identification of suitable solutions for components of the GT is nowadays becoming really challenging for the materials community. For low pressure turbine disks (LPTD) which is the main application for the AD730 alloy investigated in the present paper, the alloys must have high mechanical strength as well as thermomechanical fatigue, oxidation and corrosion resistance at temperature as high as 650°C [1] . New alloys have been identified over the past 15 years, including the γ/γ' polycrystalline superalloys such as René 65 [2], Udimet® 720 [3] and AD730 [4] alloys to replace A718, whose microstructure rapidly evolves at these temperatures, resulting in insufficient mechanical properties [5–7]. Although these new alloys satisfy the mechanical [8,9], oxidation resistance [10] and microstructural stability [11] criteria, it was observed [12] that they suffer from much severe degradation in low temperature hot corrosion (LTHC) conditions in comparison to A718, all test parameters being similar. Thus the use of new-generation of turbines raises serious questions about the ability of these parts to withstand such hot corrosion environments.

LTHC occurring in the ~ 550-750 °C temperature range, also named Type-II hot corrosion, is a well-known [13,14] issue that results from the ingestion of particles (salts, dust, ash) during aircraft operation, combined with the presence of sulfur from fuel combustion by-products in the form of SO_2(g) and SO_3(g) [15]. The interaction between the ingested particles and sulfur bearing gaseous molecules leads to the formation of sulfates (Na_2SO_4, K_2SO_4, $MgSO_4$, $CaSO_4$,...) recognized to induce severe degradation [16]. Type II corrosion attacks take the form of pitting, which can impact e.g. the fatigue strength of aerospace components. The large majority of studies of the hot corrosion resistance of alloys was carried out in the presence of pure sodium sulfate, since it was the most abundant sulfate present in the deposits according to DeCrescente et al. [16] and one of the most thermally stable sulfates. Thus lab scale and burner rig evaluation of the hot corrosion resistance of alloys generally involved NaCl or Na_2SO_4 spraying prior or sequentially during the high temperature exposure in SO_2 (g) containing atmosphere [17].

The corrosion mechanisms generally put forward to explain the attacks involve oxidation, sulfidation and fluxing of protective oxide layers [18] into the molten salts. Fluxing supposes protective oxide layer dissolution into a liquid phase. However, in some cases where no liquid phase is thermodynamically expected nor experimentally observed, severe attacks have also

been reported [19,20]. The necessity of the presence of a molten medium thus remains controversial.

The formation of low melting temperatures mixtures is mainly associated to the sulfation [21] of alloy oxidation products, when Na_2SO_4 deposit and SO_3(g) are simultaneously present. Indeed the reaction of SO_3 (g) with NiO, CoO or Co_3O_4 [22] may form $NiSO_4$ or $CoSO_4$ when the SO_3 partial pressure is high enough (> 50 ppm for Co_3O_4 at 700°C [22]). Mixing these metallic sulfates with Na_2SO_4 can result in low melting temperatures (e.g. $NiSO_4$-Na_2SO_4 and $CoSO_4$-Na_2SO_4 mixtures can melt at 671°C and 578°C respectively) [22,23]; i.e. in the LTHC domain where severe hot corrosion degradation are generally reported.

The AD730 alloy is a forged nickel-based alloy developed for current engines with optimized thermodynamic efficiency. This efficiency can only be achieved by increasing the inlet gas temperatures, thus leading to component exposed to temperatures that can exceed 650-700°C. The AD730 alloy, which contains more than 16% wt. chromium and 2% wt. aluminum, is highly resistant to oxidation in air thanks to the development of a protective Cr_2O_3 layer [10]. The mechanical properties of this alloy are ensured by the precipitation of γ'-Ni_3[TiAl] phases and by the reinforcement of the nickel-based matrix with elements such as Co, Mo, or W. The presence of these various refractory elements is reported in the literature as detrimental, particularly for resistance to hot corrosion [24,25]. The sulfation of cobalt [26] can lead, in the presence of SO_3 (g) and Na_2SO_4, to the formation of a low-melting-point mixture (as low as 587°C [23]). The refractory elements Mo and W form acidic oxides and can react with Na_2O to form mixed oxides, which also have low melting points (T_m Na_2MoO_4 = 687°C ; T_m Na_2WO_4 = 698°C [24,25]). Thus, in so-called type II hot corrosion conditions where SO_3(g) is present, the formation of a liquid phase is possible even at low temperatures.

Studies by Jones et al. [27] dealing with the hot corrosion of Co-based alloys at 700°C, observed controversial results using a mixture of Na_2SO_4-$MgSO_4$ (eutectic melting point 670°C [28]) since the use of this salt did not lead to a more severe attack than starting with pure Na_2SO_4 deposit (T_m = 884°C). At the same period [29], and later confirmed by Gheno et al.[30], the role of hot corrosion inhibitor has been ascribed to $MgSO_4$, forming MgO in basic conditions. However, in the gaseous acidic conditions of Jones (air + 250 ppm SO_2) [27], MgO was not detected in the corrosion products. Thus this study was carried out i) to clarify the necessity of a liquid phase to initiate severe attack, ii) to investigate the role of $MgSO_4$ in type II corrosion conditions, and iii) to estimate the hot corrosion resistance of a new generation AD730 alloy.

To do this, hot corrosion and sulfation experiments in presence of Na_2SO_4 and mixed Na_2SO_4-$MgSO_4$ were carried out at 650 °C and 700 °C (i.e. at temperatures respectively lower and higher than the melting point of the Na_2SO_4-$MgSO_4$ mixture).

2. Materials and Methods

2.1 Alloys

The industrial alloy AD730, dedicated to the manufacture of low-pressure turbine discs, was supplied by the SAFRAN group and was in the same metallurgical and heat treatment conditions as expected for use in service. AD730 is a γ/γ' polycrystalline nickel-based alloy produced by casting and forging. Details about its microstructure and manufacturing can be found elsewhere [31]. The composition of AD730 is given in Table 1 (in weight percent).

Table. 1. Chemical composition (in wt.%) of AD730

Element	Ni	Co	Cr	Al	Ti	Fe	Nb	Mo	W	Zr
wt%	Bal.	9.0	16.0	2.0	3.6	4.3	1.1	3.0	2.5	0.05

2.2 Corrosion tests

The guidelines of the COST program [17] were followed for conducting the hot corrosion evaluation tests. Cylindrical samples of 10 mm of diameter, 1.5 mm thick, were used. Samples were first ground to 800 grit, then pre-oxidized for 2 h at 700 °C, resulting in the formation of a thin Cr_2O_3 layer (< 1 µm) which enhances adhesion of the sulfate deposits. An amount of 1 ± 0.3 mg.cm^{-2} of dry salt was deposited on each side of the sample surfaces: spraying a Na_2SO_4 solution or a solution prepared from commercial sulfates (99% purity Na_2SO_4 and 99.5% purity $MgSO_4$ from Sigma-Aldrich) was performed, the samples being pre-heated at 250 ± 20°C on a hot plate. The proportion of Na_2SO_4 and $MgSO_4$ in the solution of salt mixture was 56/44 in mol.% respectively, corresponding to the eutectic composition in the pseudo-binary phase diagram Na_2SO_4-$MgSO_4$ [28]. Samples were then set in an alumina holder, placed in a tubular furnace fitted with a concentric quartz tube (details can be found in [21]). The heating rate was set at 10°C.min^{-1} and the test duration was 100 hours. Isothermal corrosion experiments were performed at 650°C and 700°C. The hot corrosion environment was set by incorporating in the furnace a mixture of (air + 400 ppm $SO_{2(g)}$) for a total gas flow rate of 80 ml.min^{-1}. The $SO_{2(g)}$ amount was chosen higher than 300 ppm, which is the partial pressure thermodynamically required to form a molten mixture at 700°C in the Na_2SO_4 – $NiSO_4$ system [23]. A platinum grid was placed upstream and close to the samples in order to catalyze the SO_2 oxidation and reach the O_2 – SO_2 – SO_3 equilibrium (Eq.1).

$$SO_2 + 1/2O_2 = SO_3 \qquad \Delta G_r(700°C) = -7.47\ kJ.mol^{-1} \qquad \text{(Eq.1)}$$

Mass variations were measured with a 0.1 mg precision.

2.3 Post-corrosion characterization

After corrosion tests, the samples were prepared for cross-sectional observation. Metallographic preparation was made with an ion beam polisher (JEOL CP6500), strictly avoiding the use of water. Prior to ion beam polishing, one side of the sample was embedded in a Gatan (G2) bi-component resin, and a glass slide was bonded to the resin-coated surface to protect corrosion products from mechanical stresses. Once the resin was polymerized, the samples were cut with a wire saw using an aromatics-free petroleum as lubricant.

After metallographic preparation, the samples were observed with a Field Emission Gun - Scanning Electron Microscope (FEG-SEM Thermo Fisher Scientific) with an acceleration voltage of 15 kV, and a transmission electron microscope using JEM - ARM 200F Cold FEG TEM/STEM operating at 200 kV and equipped with a spherical aberration (Cs) probe and image correctors (point resolution 0.12 nm in TEM mode and 0.078 nm in STEM mode). For TEM investigations, cross-sections of the corrosion layers were obtained by thin TEM-foils from the corroded samples with a dual focused ion beam (FIB) scanning electron microscope (Helios Nanolab 600i) using the in-situ lift-out technique. EDX analyses were performed in STEM mode, using Centurio Silicon Drift Detector (SDD) that collects X-rays at large solid angle of up to 0.98 steradians from a detection area of 100 mm^2. To obtain accurate information on the elemental distribution in the corrosion products, X-ray mapping was performed using Castaing microprobe (JEOL JXA-8530) at 15 kV. The nature of the chemical species present in corrosion products was identified using wavelength X-ray dispersion spectrometer (WDX), because of the low resolution of energy dispersive detectors (~50-100 eV), meaning that X-rays from niobium (E(Lβ) = 2.257 keV), molybdenum (E(Lα) = 2.293 keV) and sulfur (E(Kα) = 2.307 keV) cannot be correctly separated without a loss of spatial resolution with EDX technique. WDX spectrometry solved the Mo and S interference problems, owing to its higher energy resolution.

3. Results

3.1 Corrosion tests results

Figure 1 shows the specific mass change for AD730 after 100 h in air + 400 ppm SO_2 at 650°C and 700°C in the presence of Na_2SO_4 and the Na_2SO_4-$MgSO_4$ mixture. For a reminder, at 650°C

both salts are initially solid, while at 700°C the Na_2SO_4-$MgSO_4$ deposit is expected to be molten. The data presented in Figure 1 correspond to the average of three and two samples at 650°C and 700°C, respectively.

Mass variations are broadly comparable for both salts at 650°C, and the order of magnitude is around 1.05 ± 0.2 mg.cm^{-2}. In comparison, the mass gain of this alloy [10] due to pure oxidation in this temperature range in air is less than 0.1 mg.cm^{-2} after 100 hours. At 700°C, mass variations are significantly greater with 10.2 ± 2.3 mg.cm^{-2} at 700°C for the Na_2SO_4 salt and 4.9 ± 0.5 mg.cm^{-2} for the mixture. Thus, although the sulfate mixture (Na_2SO_4-$MgSO_4$) is liquid at this temperature, samples corroded with the mixture take up around half the mass of those in contact with the Na_2SO_4 deposit. The surface aspect of the samples is also different. It is brown after treatment at 650°C, whereas a green colored surface is observed at 700°C, with some spallation for the samples corroded with Na_2SO_4.

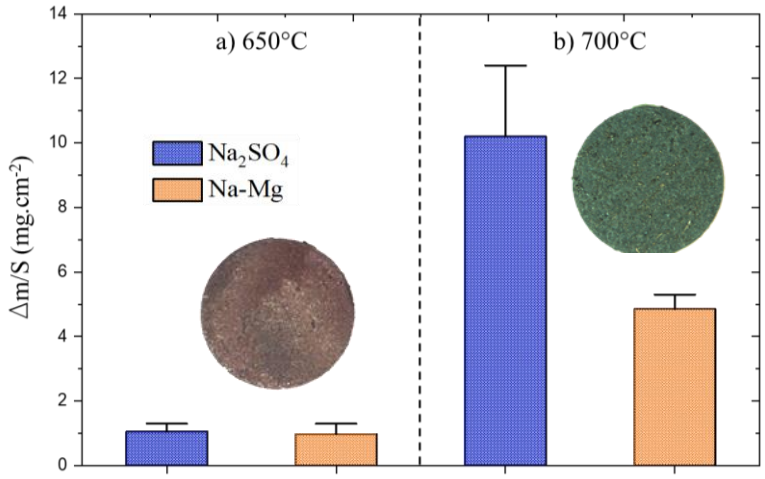

Figure 1: Specific mass variations of AD730 after 100 h in air + 400 ppm SO2 with 1 mg.cm^{-2} deposit of Na_2SO_4 (in blue) or Na_2SO_4-$MgSO_4$ (in orange) mixture at a) 650°C and b) 700°C

3.2 Cross section observation

Figure 2 shows the cross section micrographs for samples exposed at 650°C and 700°C in the presence of the Na_2SO_4 deposit and of the Na_2SO_4-$MgSO_4$ mixture. Consistently with the mass change, the severe corrosion attack at 700°C was obvious, especially for the alloy exposed to the Na_2SO_4 deposit.

At 650°C, the corrosion features were different for the tests with Na_2SO_4 and Na_2SO_4-$MgSO_4$ mixture. The cross section of the sample exposed to Na_2SO_4 deposit (Fig. 2a) exhibits a higher surface fraction of pitting than the section of the sample exposed to the mixture. The pits depth is of the same order of magnitude (around 5 µm) in both cases. The initial interface of the

AD730 sample remains perfectly flat after the exposure to the mixture; opposite to the surface of the sample corroded with Na_2SO_4.

For the mixture, a very thin chromium-rich layer (see green arrows Figure 2b) is still visible at the metal-salt interface, most probably corresponding to the layer initially formed in air during the pre-oxidation stage. For the Na_2SO_4 salt, this layer is totally substituted by thick Cr-rich corrosion products.

The outer part of the salts also contains some veins and fine precipitates of nickel-, iron- and cobalt-rich mixed oxides for both salts. These oxides form the light border, in the outer part of the salt; this border is obvious in the case of the sulfate mixture; but less with the Na_2SO_4 salt. EDX measurements also evidence that the amount of nickel in the salt is much higher in the case of the Na_2SO_4 salt than for the sulfates mixture: 23.5 at.% vs 4.6 at.% respectively. In both cases, the internal part of the pits displays two different grey levels. The part located at the interface is darker, showing this part is either enriched with low Z atoms or is less dense in comparison to the part situated just above which appears brighter in back-scattered electrons mode. These pits are further described hereafter with HR-TEM characterization.

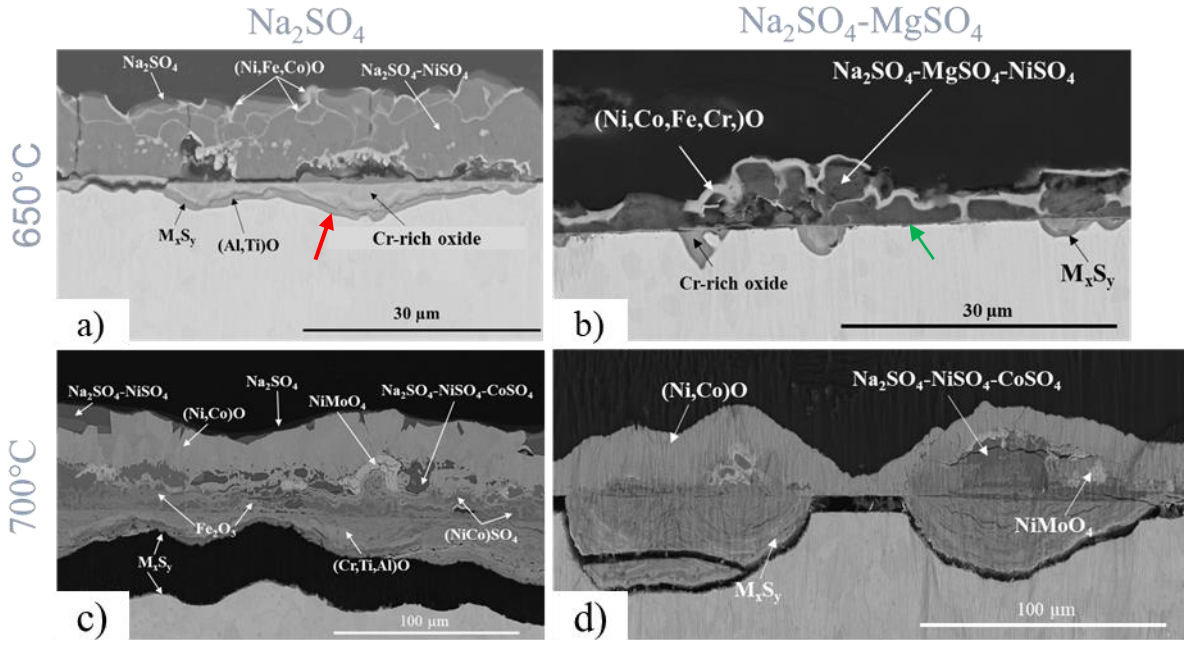

Fig. 2: Cross-sections (SEM-BSE) of AD730 alloy after 100 h exposure in air + 400 ppm SO_2 at 650°C and 700°C with 1 mg.cm^{-2} of Na_2SO_4 (a and b) and Na_2SO_4-$MgSO_4$ (c and d). The green arrow locates the very thin chromium-rich layer. The red arrow corresponds to the location where the FIB lamellae (Fig. 4) was collected.

Interestingly, a very thin, nickel-free Na_2SO_4 layer of approximately 700-800 nm in thickness covers the top surface. It is not clearly observed for the Na_2SO_4-$MgSO_4$ mixture at these magnifications.

At 700°C (Fig. 2c and 2d), the damage is clearly more pronounced and the corrosion products tend to spall off during sample handling. The thickness of the corrosion products reaches 60-100 µm. As at 650°C, the morphology of the attack differs between both salts. While with Na_2SO_4 the attack leads to a generalized and severe consumption of the alloy, the cross section of AD730 corroded with the sulfate mixture "only" exhibits localized corrosion, forming pits. The initial sample interface is clearly visible in these SEM micrographs allowing the measurement of the depth of attacks; it reaches up to 50 µm for both cases; *i.e.* the difference in mass change noticed in Fig.1 is related to the affected surface fraction and not to the depth of the attack.

The clear evidence of the initial alloy interface also allows the description of the corrosion products in terms of an outer layer and an inner layer.

With Na_2SO_4, the extreme surface is covered by a thin "pure" Na_2SO_4 layer, similarly to that observed at 650°C. In the outer layer, a thick layer (~25-30 µm) of coarse-grained (Ni,Co)O, embedded in Na_2SO_4 - $CoSO_4$ - $NiSO_4$ mixture, developed. In this outer part of the corrosion products, $NiMoO_4$ crystals are noticed just beneath (Ni,Co)O as well as crystals of $(Ni,Co)SO_4$ mixed sulfate. Layers of iron-rich oxides, formed between the outer (Ni,Co)O layer and the inner layer. The latter is made up of a series of chromium enriched layers (Fig. 2c and 2d); which will be further characterized in the following.

With the Na_2SO_4-$MgSO_4$ mixture, the top surface consists in a dense and continuous (Ni,Co)O oxide layer. The amount of sulfate in the corrosion products is clearly lower than for Na_2SO_4. With the mixture, salt residues were found between the (Ni,Co)O top layer and the inner layer. Except these two differences in terms of sulfate amount and location of the salt, the stratification and order of oxides and corrosion products is similar to the one observed at 650°C. This is further described below.

3.3 WDX analysis of corrosion products

The results for the test carried out at 700°C with the Na_2SO_4-$MgSO_4$ mixture are given in Figure 3. X-ray elemental maps were recorded to accurately determine the distribution of the alloy's major elements (Ni, Co, Fe, Cr), of minor elements (Al, Ti, Nb, W), of sulfate-related elements (Na, Mg, S) and finally of Mo. Corrosion products being very similar to those obtained with

the pure Na_2SO_4 deposit, the corresponding results are not presented here. To follow the description given below, it should be noted that sample preparation, using ionic polishing, leads to an artifact that is difficult to avoid due to the redeposition of metallic atoms during ion beam etching at the spalled interface.

First, the elemental maps distinctly shows the difference of composition of the inner and outer layers previously described. The straight interface separating the outer and inner parts of the corrosion products, and corresponding to the initial alloy interface, is obvious on the Nb elemental map.

The outer part consists mainly of the Ni, Fe and Co oxides with some Mo-rich compounds. Co and Ni form the outermost layer. Chromium is strongly enriched in the inner part. Al, Ti, Nb and W are also mainly found in the inner part, but Al is interestingly distributed both at the alloy-corrosion products interface and in the outer part, close to the initial alloy interface. A Na_2SO_4 thin layer is present at the external top surface (Na X-ray map, Fig. 3b) , as it is for the corrosion in presence of pure Na_2SO_4 (Fig. 2a and 2c).

As evidenced with the comparison of S and Mo maps, the location of these elements is different, showing the benefit of WDX spectrometry. Molybdenum forms oxides in the outer part and also slightly accumulates at the alloy-corrosion products interface. The comparison of the S, Mo and O elemental maps highlights the location of the two sublayers developing in the inner part of the pit.

The Mo and S rich layer close to the alloy-corrosion products interface is clearly O-depleted suggesting that this layer is mainly a sulfide-rich layer, whereas the outer part mainly consists of oxides. This difference of chemical composition is also associated with the location of Mg and Na, which are mainly present in the outer layer of the inner part. The comparison of S, Mg and Na maps with the chromium map indeed evidences that S, Mg and Na alternate with chromium-rich layers. The distribution of magnesium is clearly localized, while that of sodium is more diffuse in the inner part of the pit. In the sulfur-rich zone close to the alloy interface, magnesium and sodium are no longer present, but the W, Nb, Mo heavy elements as well as Al and Ti are enriched.

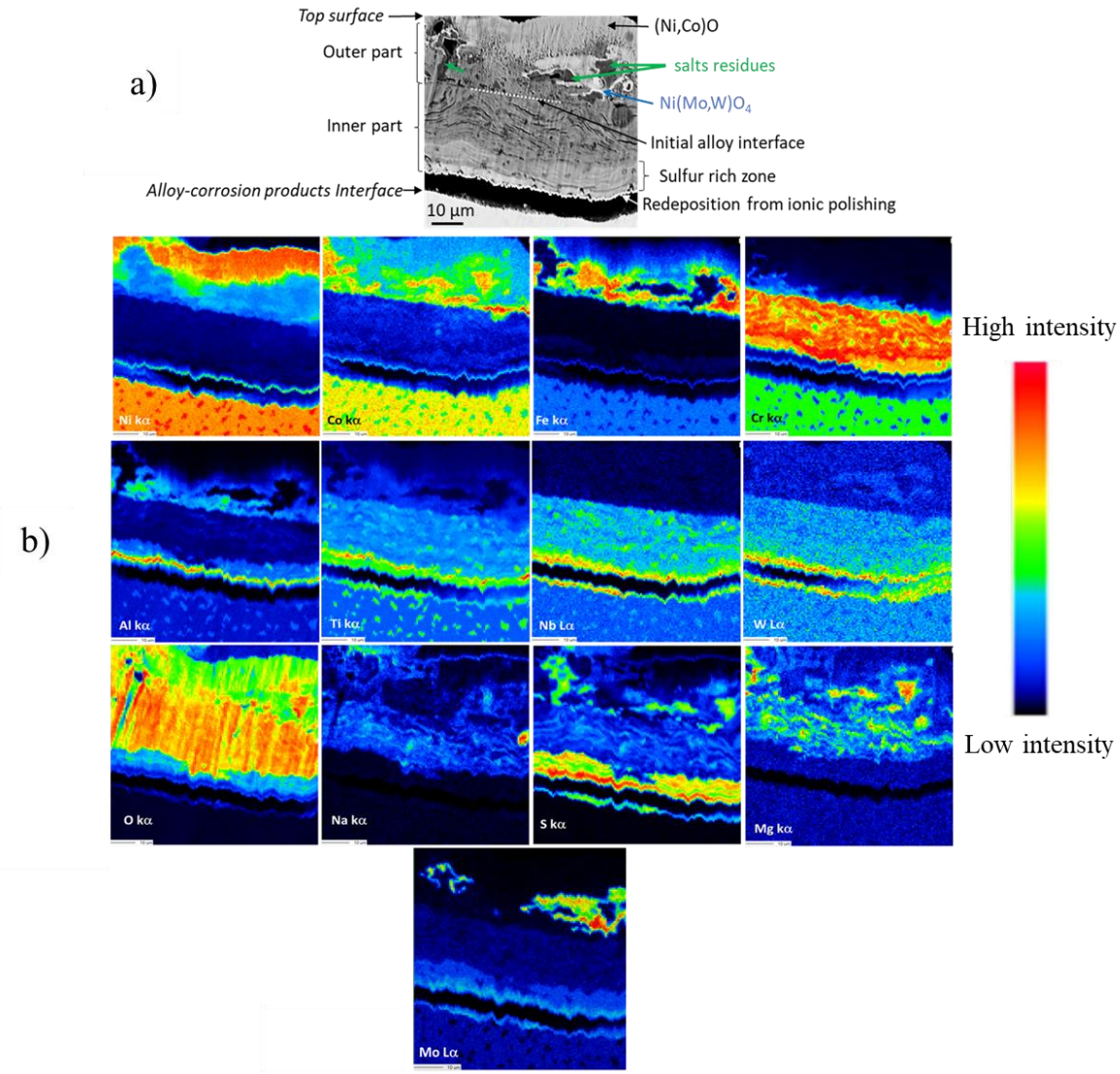

Fig. 3: AD730 after 100 h exposure at 700°C in air + 400 ppm SO_2 with Na_2SO_4-$MgSO_4$ deposit. a) overview BSE micrograph of the cross section and b) Elemental maps obtained with the Castaing microprobe

3.4 High resolution characterization of the corrosion products

To get further information on the nature of the corrosion products formed in the pits, a FIB lamellae was picked up from the AD730 sample corroded at 650°C in the presence of Na_2SO_4. Figure 4 displays a general view of the lamellae as well as the electron diffraction patterns (Selected Area Electron Diffraction - SAED) of the three identified parts. The two sublayers situated in the inner part of the pit and discussed in section 3.3 with elemental maps (Fig. 3), are clearly evidenced defining Zone 1 and Zone 2 for the S-rich and the Cr-rich zones, respectively.

Zone 1 at the interface with the alloy, which appears dark in BSE imaging (Fig. 2a and 2b), is clearly highlighted using the High Angle Annular Dark Field (HAADF) detector (Fig. 4a). Its thickness is globally continuous (around 0.4 to 0.8-µm thick). The HAADF detector is highly sensitive to Z (atomic number) contrast. Heavy elements are strongly diffracted, forming bright zones at the opposite to light elements. In the present case, this imaging clearly shows the porous nature of the inner layer. These pores are distributed at the metal-corrosion product interface. The microstructure in Zone 2 (Fig.4a, zone 2) is denser and brighter, characterizing the higher density and the presence of elements with a higher Z in average than in Zone 1.

For both zones, SAED shows a high number of discrete diffraction spots as well as rings connecting the spots, evidencing the polycrystalline nature of the corrosion products (Fig.4b and 4c). The presence of an amorphous phase cannot be ruled out in view of the diffuse ring close to the direct beam central position. For Zone 1, Al_2O_3 (corindon R-3c), TiO_2 (rutile $P4_2/mnm$) and WS_2 ($P6_3/mmc$) diffraction patterns are identified, whereas Cr_2O_3 (eskolaite R-3c) and TiO_2 (rutile $P4_2/mnm$) are observed in Zone 2.

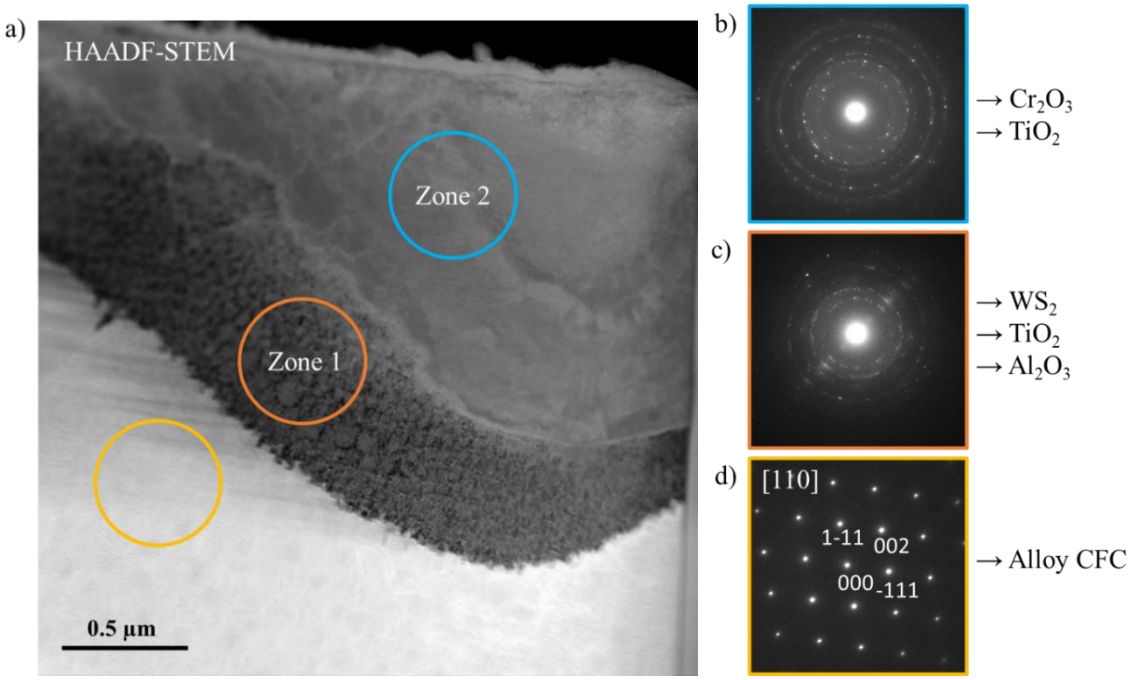

Fig. 4: Cross-section characterization of AD730 alloy exposed for 100 hours at 650°C in the presence of Na_2SO_4 under air + 400 ppm SO_2: a) STEM-HAADF image and electron diffraction (SAED) images taken - b) in zone 2, c) in zone 1 and d) in the substrate (indexed for the face-centered cubic structure (Fm-3m) of Ni along the zone axis [110])

Fig. 5 shows Bright Field (BF) and High Resolution Transmission Electron Microscopy (HRTEM) images of the metal – corrosion products interface. The interface looks like a staircase where WS2 platelets are located. The pores discussed above for Zone 1 are related now to the bright areas in the BF mode. The layer in Zone 1 can be described according to a mixture of more or less spherical light grey particles of 100-200 nm in diameter and others objects with an acicular morphology. These latter appear in the form of stacked sheets and corresponded to WS2 crystals (white arrows). The bidimensional feature of the latter compound is obvious in Fig. 5c.

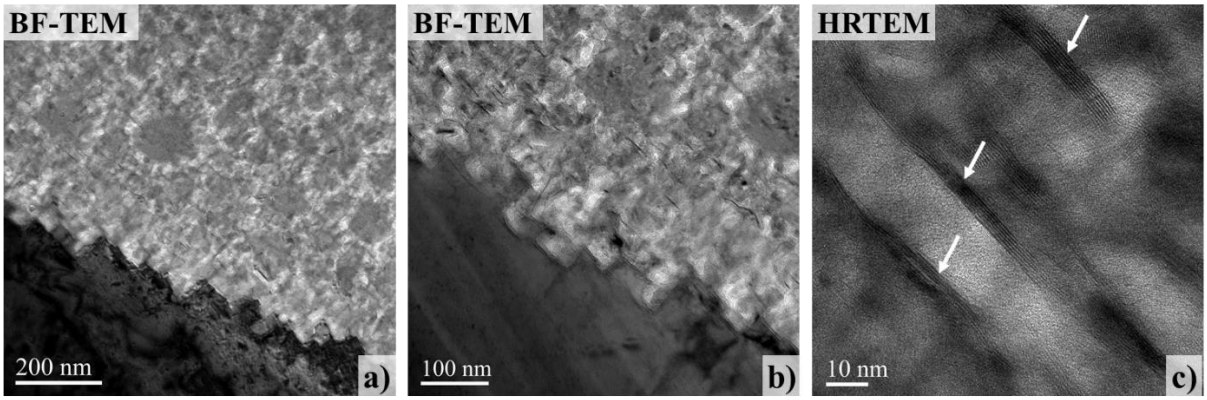

Fig. 5: Bright Field and HRTEM images of Zone 1 at different magnifications. White arrows indicates the WS_2 bidimensional crystals

X-ray mapping (EDS-STEM) was carried out (Fig. 6) on this section; Fig. 6b shows an overview of the investigated section in bright field mode, with the unaffected alloy located at the bottom, Zone 1 in the middle, and Zone 2 at the top of the micrograph. Fig. 6a displays an overlay of the X-ray maps of Na, S and O, clearly showing the difference in composition between Zone 1 and Zone 2. The blue color shows Zone 2 consists of a rich oxide scale. Chromium (in red in Fig. 6c) and titanium (in green) are mainly located in Zone 2. But unlike Cr, Ti is also present in Zone 1. The latter is enriched with Na and S, but some O remains. Chromium sulfide can also be observed in red color in Fig.6c (white arrow). The dark band at the substrate-Zone 1 interface, ~150 nm thick, in Fig. 6c (white square), corresponds to an Al enriched layer, labelled Al_2O_3 in Fig. 8a. This location is further described in the following.

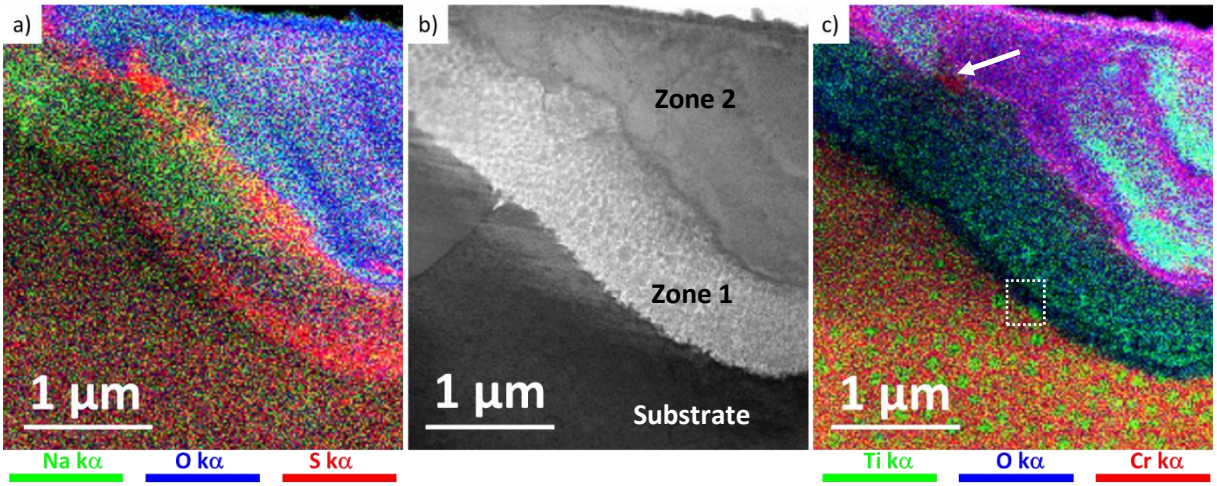

Fig. 6: STEM-EDS mapping of the cross-section of AD730 at 650°C after 100 hours of exposure to 400 ppm SO_2 in the presence of Na_2SO_4 a) overlay of Na-O-S X-ray elemental maps, b) bright field image and c) overlay of Ti-O-Cr X-ray elemental maps

Fig.7 shows an overlay of the Ti, S and Cr elemental maps. Fig.8a and 8b present the overlays of the Al-Ni-Cr and O-Al-S X-ray maps, respectively. These chosen superpositions highlight that the dark band at the substrate-Zone 1 interface mainly contains sulfur and aluminum. Oxygen is also systematically associated to aluminum in these products located close to the alloy interface, as evidenced in Fig. 8b, where the nanosized Al_2O_3 correspond to the light blue rounded particles. Spherical objects correspond thus to aluminum oxides. The distribution of these oxides and their morphologies look to broadly follow that of the γ' precipitates initially present in the microstructure of the AD730 alloy.

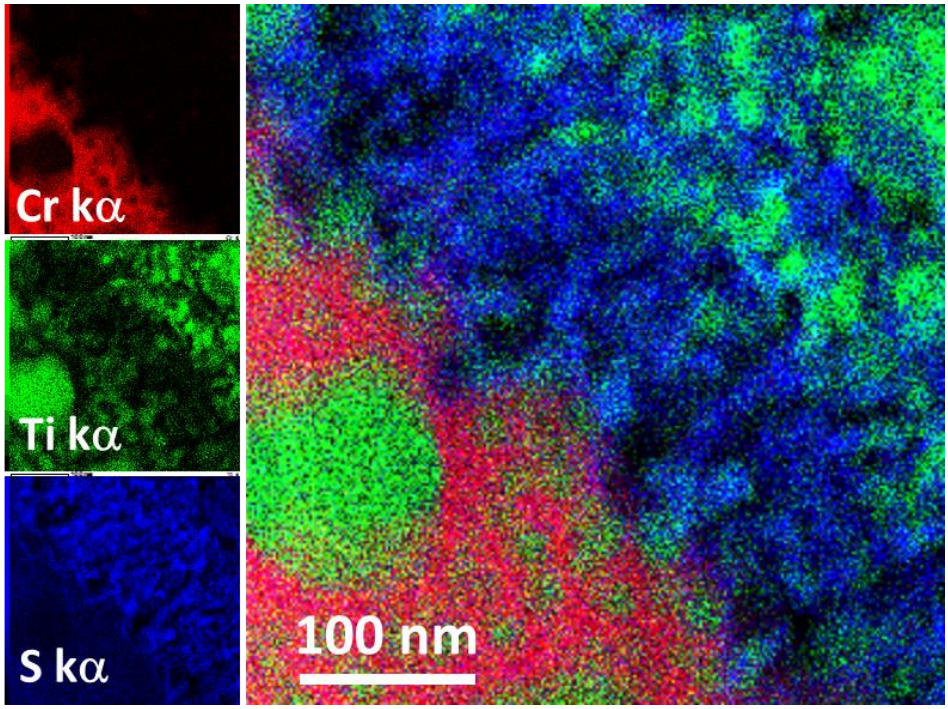

Fig. 7: STEM-EDS mapping of the cross-section of AD730 at 650°C after 100 h of exposure in air + 400 ppm SO_2 with a Na_2SO_4 deposit – Region of the interface - Overlay of the Cr-Ti-S X-ray maps

Fig.7 also evidences that Ti did not accumulate in this area but further away from the interface. The yellow sticks at the interface, Fig. 8b and highlighted with white arrows, show the WS_2 precipitates outlining the stairs of the interface. The overlay of W and S is supplied in Supplementary Material. In the latter, as well as in Fig. 8b, it is obvious that sulfur in some places cannot be associated to a metallic element. Sulfur appears in pure red in Fig. 8b and in pure blue in Supp.Mat.1. Thus the formation of pure sulfur, as an intermediate compound, cannot be ruled out of the corrosion mechanism.

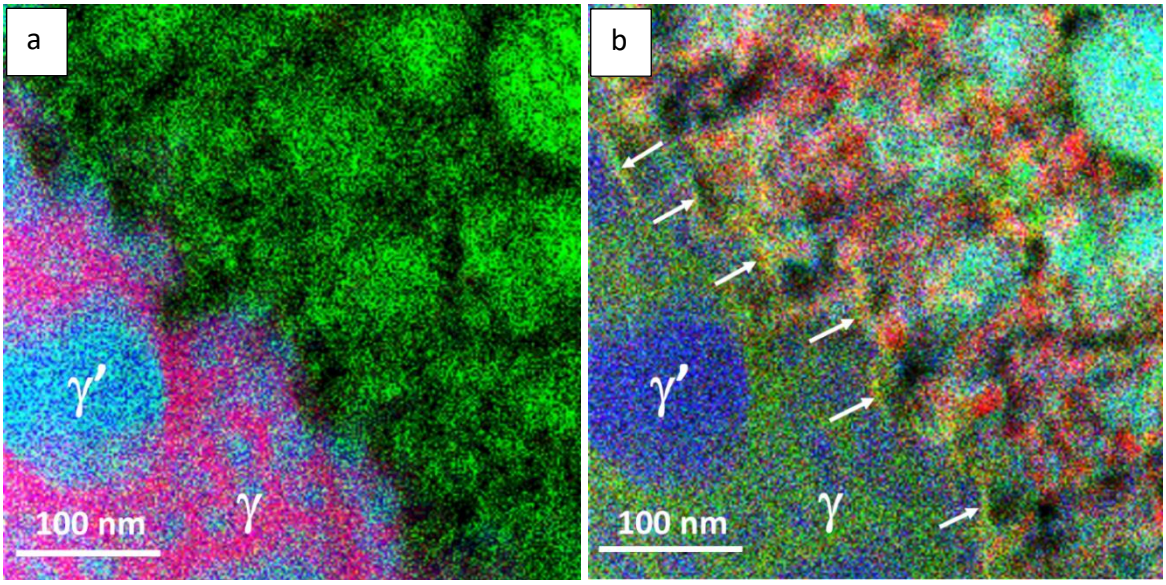

Fig.8: Overlay of the a) Al-Ni-Cr (in green, blue and red colors, respectively) X-ray maps, and b) O, Al and S (in green, blue and red colors, respectively)

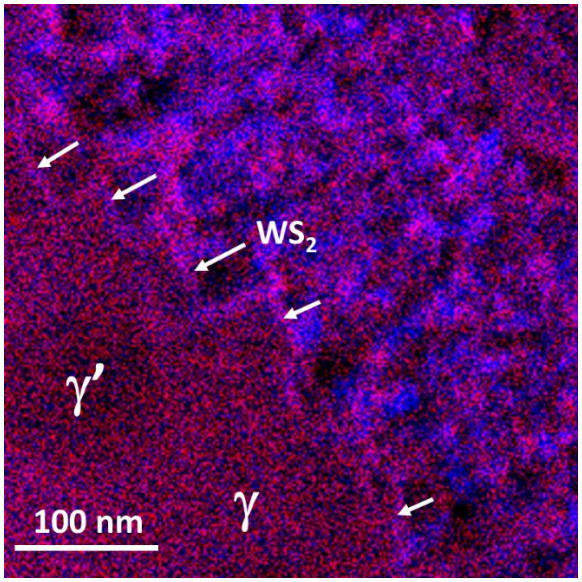

Supp.Mat.1: STEM-EDS mapping of the cross-section of AD730 at 650°C after 100 h of exposure in air + 400 ppm SO_2 with a Na_2SO_4 deposit- Overlay of the a) W (in red) and S (in blue) maps

4. Discussion

In this study, two environments (Na_2SO_4 and the Na_2SO_4-$MgSO_4$ mixture) and two temperatures (650°C and 700°C) were investigated to evaluate the oxidation behavior of the AD730 alloy in (air + 400 ppm of SO_2) atmosphere. Type II corrosion primarily leads to the formation of pits whose morphology and depth could significantly affect the mechanical properties of structural components [32]. It is therefore important to identify the mechanisms ruling the pits growth in order to limit this kind of degradation. A $MgSO_4$-Na_2SO_4 mixture is used here in order to evaluate the role of $MgSO_4$ in Type II corrosion, given that these sulfates are also present in the deposits observed on aeronautical components [16]. The influence of the presence of a liquid phase from the very beginning can also be evaluated by using this mixture, since its melting temperature is 670°C.

4.1 Influence of the salt composition

The partial substitution of sodium by magnesium in the sulfate deposits leads to a decrease of the melting temperature of the salt (670°C vs 884°C). In addition to this physical characteristic change, it has also been shown [33] that the mixture has more acidic properties than sodium sulfate. This acidic character can be explained by the dissociation pressure of $MgSO_4$, which is several orders of magnitude higher than that of Na_2SO_4. The free enthalpies and partial pressures associated with the decomposition equilibrium of sodium sulfate and magnesium sulfate at 700°C are given in Table 2. This difference could therefore promote dissolution by acidic fluxing of the protective layers; chromia Cr_2O_3 in the case of AD730 [12].

Table 2: Dissociation pressures of $MgSO_4$ and Na_2SO_4 at 700°C [34–37]

Reaction	$\Delta G^{\circ}(700°C)$ kJ.mol^{-1}	$P_{SO_3(g)}$ atm.	Ref.
$MgSO_4 = MgO + SO_3$ (g)	109.5	1.3 x 10^{-6}	[34,37]
$Na_2SO_4 = Na_2O + SO_3$ (g)	413.9	6.0 x 10^{-23}	[35,36]

Consistently with these thermochemical data, both sulfates used for the present study are thermodynamically stable in the conditions used for the present tests; i.e., under partial pressures of 0.2 atm. O_2 (g) and ~ 2.0 10^{-4} atm SO_3 (g).

Despite these differences in the physicochemical properties of the two salts, the overall mass variation of the samples is broadly the same for both types of deposit in tests conducted at a temperature of 650°C. These similar mass gains raise questions, given that a certain degree of variability would have been expected given the localized nature of the pitting corrosion. The

hypothesis that the composition of the test atmosphere has a major influence on degradation rate cannot therefore be rejected. Nevertheless, the form of the attacks at 650°C is slightly different, as the pitting is more widespread when Na_2SO_4 salt is used. In addition, the observed corrosion products (Fig. 2a and 2b) are very different in the case of exposition to Na_2SO_4 salt compared to the mixture. With Na_2SO_4, the proportion of sulfate on the surface of the sample increases, showing the sulfation of nickel oxides and their dissolution in Na_2SO_4. Conversely, nickel oxides are observed in the case of the Na_2SO_4-$MgSO_4$ mixture.

At 700°C, the mass gain of the AD730 alloy is higher regardless of the salt. However, the attack is widespread and the amount of salt on the surface of the alloy after corrosion is very high with Na_2SO_4 salt, whereas it remains low with the Na_2SO_4-$MgSO_4$ mixture. For the latter, corrosion always occurs in the form of pitting.

In order to assess whether the nature of the salt could influence the equilibrium of the sulfation reaction of nickel and cobalt oxides, tests in the presence of SO_3 (g) with thermogravimetric monitoring were carried out with the two salts.

The sulfation of high purity MO oxides (NiO 99.998%; CoO 99.99% from Alfa Aesar) were continuously followed during 24 h using a thermobalance (SETARAM - KEP Technologies) designed to withstand corrosive gases [21]. 5 g of two mixtures, composed of 40 MO – 60 Na_2SO_4 and 40 MO – 33.6 Na_2SO_4 – 26.4 $MgSO_4$ (mol.%.), respectively, were prepared from oxide and sulfate powders. The 33.6 Na_2SO_4 – 26.4 $MgSO_4$ mix corresponds to the composition at the eutectic (56 – 44 [30]). Once manually blended together in an agate mortar for ten minutes, the powder mixes were stored in an oven at 120°C before the thermogravimetric measurements. A platinum crucible was filled with a sampling of around 25 mg of the powder mix described above. The details of the apparatus can be found in [22]. The total gas flow (air + 1000 ppm SO_2) passing through the quartz tube was 40 ml/min. The catalysis of the SO_2 oxidation into SO_3 (Eq. 1) was allowed by both platinum made hanging system and the crucible itself. The results in Fig. 9. are reported in moles of SO_3 (g) adsorbed per mole of oxide according to Eq.2.

$$MO + SO_3\,(g) = MSO_4 \qquad \text{Eq.2}$$

These results show that the sulfation of NiO and CoO oxides readily occurs in these conditions from the earliest minutes of the exposure. In both cases, the sulfation does not reach 100% of completion, probably because of a sintering effect of the initial oxide powder. These results also evidence that mass changes are significantly affected by the presence of $MgSO_4$, they are

systematically lower with the Na_2SO_4-$MgSO_4$ mixture than with Na_2SO_4; all other parameters being similar.

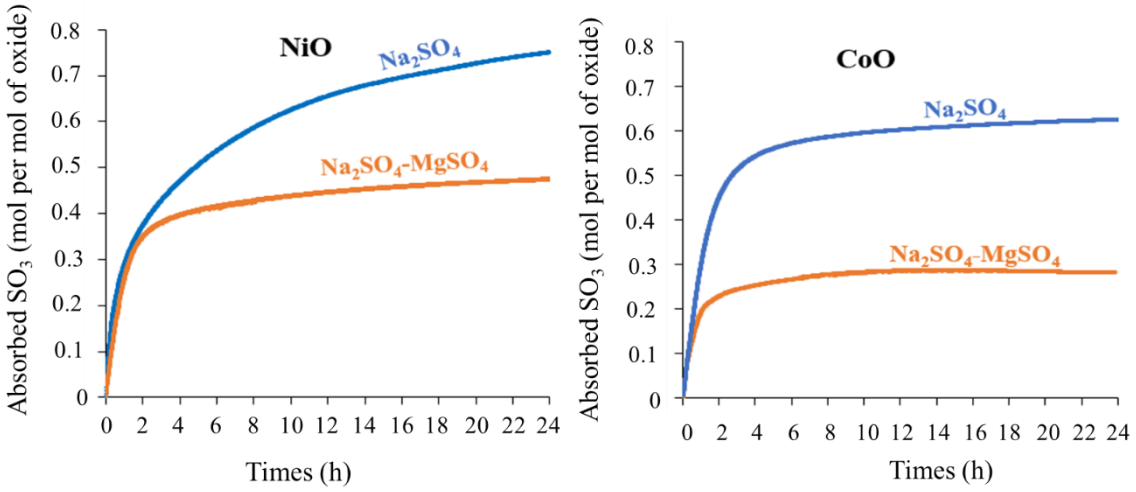

a) b)

Fig. 9: Mass gain vs. time of MO + Na_2SO_4 (40%mol/60%mol) and MO + Na_2SO_4-$MgSO_4$ (40%mol/60%mol) mixtures at 650°C for a) NiO and b) CoO under air + 1000 ppm SO_2. Results are reported per mole of sulfated oxide according to the reaction MO + SO_3 (g) = MSO_4

As a consequence, NiO and CoO is less prone to sulfation in presence of the Na_2SO_4-$MgSO_4$ mixture than when pure Na_2SO_4 is used. This trend is in agreement with the observation of a lower amount of salt at the top surface of AD730 after the 100 h exposure to the Na_2SO_4-$MgSO_4$ mixture, and also with the experimental data of Jones et al. [27]. The reason why $MgSO_4$ limits the sulfation reaction of NiO and CoO is presently not understood. These results also evidence that the presence of a molten sulfate strongly enhances the degradation rate of AD730, but this degradation rate can be strongly influenced by the chemical nature of the melt.

4.2 Characterization of the corrosion products and of the oxidation mechanisms

The elemental map shown in Figure 3, and also the TEM mapping, reveal the specific positions occupied by the various oxides in the corrosion products. Malacarne et al. [12] have explained that these specific positions are related to the minimum solubility of each oxide in the molten sulfate [12,35,37]. The stratification of oxides, ranging from basic oxides (NiO, Co, and Fe_2O_3) at the external interface of the corrosion products to acidic oxides (Cr_2O_3, Al_2O_3, and TiO_2) at the internal interface, indicates a decreasing gradient of oxide ion O^{2-} concentration from the external part of the deposit to the internal interface. The observations made in the present work do not challenge the conclusions and the mechanism established by Malacarne et al. [12]. In this mechanism, based on the high ionic and electronic conductivities of species in the molten salt, the oxidation and reduction reactions predominantly occur at the metal-oxide and oxide-

gas interfaces, respectively: the oxidation of the metallic species occurs at the metal-oxide interface, and the reduction of SO_3/O_2 occurs at the oxide-gas interface. Consequently, the amount of SO_3 (g) at the reactive external interface should govern the degradation rate, as previously shown by Kistler et al. [19]. SO_3 is also reputed responsible for the sulfation of oxides, particularly promoting the oxidation of Ni and Co elements [12]. The as-formed nickel and cobalt sulfates contribute further to sustain the molten salt fraction in the corrosion products. In the present study, the limitation of the sulfation of these oxides seems to be a key point to explain the difference of corrosion behavior between exposures to Na_2SO_4 and Na_2SO_4-$MgSO_4$ mixture at 700°C.

Thus, once the process initiates, all constitutive elements of the AD730 alloy oxidize and form metallic ion M^{n+}. The oxide ion concentration should be very poor at this location; i.e. the pit floor acidifies. With the oxide ion concentration increasing toward the surface, the oxides Al_2O_3, TiO_2, then Cr_2O_3, which present a low solubility in acidic environments [18], precipitate. The other cations continue their migration towards the external part of the corrosion products - where the oxide ion concentration is the higher -, forming sequentially the oxides Fe_2O_3, then NiO and finally CoO. This fast migration of metallic ions over tenth of micrometers suggests that transport in the molten salt occurs under polarization.

The high resolution characterization of the corrosion products carried out in the present work leads to additional information. It is indeed observed that the interior of the pits can be divided in two zones: the central zone of the pit is composed chromium- and titanium-rich layers between which sodium and magnesium sulfates are located, whereas the pit floor close to the alloy interface is rather enriched with tungsten and molybdenum sulfides, and aluminum and titanium oxides (Fig. 3; Fig. 7 and Fig. 8). The high resolution images clearly show round-like Al_2O_3 precipitates; i.e. that the formation of a protective Al_2O_3 layer is not possible in the present corrosion conditions. The formation of a sulfide-rich layer at the metal-oxide interface is mainly due to the low partial pressure (P_{O_2}) prevailing there. Indeed the sulfides can only be observed for thermodynamic reason in regions with low oxygen partial pressure. The geographical separation between oxide and sulfide zones demonstrates the presence of the oxygen partial pressure gradient superimposed on to the oxide ion concentration gradient. The lamellar compound WS_2 is clearly observed right at the interface with the alloy forming a stairs-like interface. This bidimensional compound is also evidenced in the hot corrosion products of DS200+Hf in quite similar corrosion conditions [20]. Surprisingly the high resolution images also show that sulfur is not associated to an other metallic specie in the vicinity of the interface

with the alloy (Fig. 8b), suggesting that pure sulfur might form in these area; i.e. that sulfur activity can be as high as unity at the alloy-corrosion product interface.

In these conditions, the formation of metallic sulfides might be an intermediate stage which hinders the formation of the continuous and protective oxidation layer. However, no proof of formation of sulfides with other elements than W and Mo was obtained. At the opposite, HR TEM observations evidence the presence of porosity directly at the interface. They could result from the volume change associated to the oxidation of the sulfides, as suggested by Young et al. [38]. The volume per mole of W in WS_2 (32.2 $cm^3.mol^{-1}$ [36]) is greater than the volume per mole of W in WO_2 (20.1 $cm^3.mol^{-1}$ [39]). Tungsten occupies more volume in WS_2 than in WO_2, thus the oxides formed by this process might lead to the formation of porosity. However, the size of the pores and the morphology of the interface does not seem compatible with just a phase transformation of the sulfides, these pores appearing much larger than the observed sulfides. These pores could thus originate from the flow of metallic species (Kirkendall effect) towards the external interface.

Conclusions

The study of type-II corrosion of AD730 was conducted in the presence of Na_2SO_4 and of a Na_2SO_4-$MgSO_4$ mixture at 650°C (both salts being solid) and at 700°C (the mixture being liquid and Na_2SO_4 being solid) under an atmosphere of air + 400 ppm SO_2. These conditions allowed the evaluation of the mode of action of $MgSO_4$.

The presence of a liquid phase from the very beginning in the cases where Na_2SO_4-$MgSO_4$ mixture was employed is not a prerequisite for the development of hot corrosion pits. However, the nature of the metal cation (Na, K, Mg, Ca) appears to be important to consider.

In the presence of magnesium sulfate, the sulfation reaction of nickel and cobalt oxides is lower than in the presence of Na_2SO_4 alone. The corrosion rate, related to the sulfation of NiO and CoO oxides, is reduced by the inhibition of this reaction, leading to less severe corrosion when $MgSO_4$ is present. The low sulfation in presence of $MgSO_4$ may be related to the thermodynamic of the $NiSO_4$-Na_2SO_4-$MgSO_4$ system, but further work has to be carried out to fully understand this effect.

The characterization of corrosion products has confirmed that the pitting propagation mechanism is based on electrochemical reactions occurring at two distinct interfaces. The low partial pressure of oxygen at the metal-oxide interface allows the formation of sulfides and/or

sulfur, thus suggesting that sulfides can be a reaction intermediate. The involvement of these sulfides in the mechanism, however, is not definitively established. Pores also formed at this interface. These observations mainly evidenced why no protective oxide layers can develop at the oxidation front.

Acknowledgements

The SAFRAN Group is gratefully acknowledged for supplying samples.

Declaration of Conflicts of interest

The authors declare that they have no known competing financial interests or personal relationships that could have appeared to influence the work reported in this paper.

Availability of data and material

The raw/processed data required to reproduce these findings can be shared on demand.

References

[1] T.M. Pollock, S. Tin, Nickel-Based Superalloys for Advanced Turbine Engines: Chemistry, Microstructure and Properties, J. Propuls. Power 22 (2006) 361–374. https://doi.org/10.2514/1.18239.

[2] C. Romain, Multiscale approach of the stress-assisted oxidation of nickel-based superalloys : from strain localization to the onset of mechanochemical damage, thesis, Universié de Toulouse, (2022).

[3] H. Monajati, M. Jahazi, R. Bahrami, S. Yue, The influence of heat treatment conditions on γ′ characteristics in Udimet® 720, Mater. Sci. Eng. A 373 (2004) 286–293. https://doi.org/10.1016/j.msea.2004.01.027.

[4] A. Devaux, B. Picqué, M.F. Gervais, E. Georges, T. Poulain, P. Héritier, AD730^{TM} - A New Nickel-Based Superalloy for High Temperature Engine Rotative Parts, in: ResearchGate, 2024. https://doi.org/10.7449/2012/Superalloys_2012_911_919.

[5] R. Schafrik, R. Sprague, "Saga of Gas Turbine Materials: Part III," Advanced Materials and Processes, 162 (2004) 27–30.

[6] J.W. Brooks, P.J. Bridges, Metallurgical Stability of Inconel Alloy 718, in: ResearchGate, 1988: p. pp 31-41. https://doi.org/10.7449/1988/Superalloys_1988_33_42.

[7] A. Devaux, L. Nazé, R. Molins, A. Pineau, A. Organista, J.Y. Guédou, J.F. Uginet, P. Héritier, Gamma double prime precipitation kinetic in Alloy 718, Mater. Sci. Eng. A 486 (2008) 117–122. https://doi.org/10.1016/j.msea.2007.08.046.

[8] J.A. Heaney, M.L. Lasonde, A.M. Powell, B.J. Bond, C.M. O'Brien, Development of a New Cast and Wrought Alloy (René 65) for High Temperature Disk Applications, in: 8th Int. Symp. Superalloy 718 Deriv., John Wiley & Sons, Ltd, 2014: pp. 67–77. https://doi.org/10.1002/9781119016854.ch6.

[9] D. Locq, C. Ramusat, J.-M. Franchet, A. Devaux, Coarse grain C&W AD730 disk superalloy for high temperature applications, in: JOURNEES Annu. SF2M, PARIS, France, 2019. https://hal.science/hal-02486871 (accessed March 4, 2025).

[10] R. Malacarne, S. Mathieu, L. Aranda, M. Vilasi, C. Desgranges, S. Knittel, Long-term isothermal oxidation behavior of two industrial polycrystalline nickel base alloys in air at 700 °C – Evaluation of intergranular oxidation distribution and kinetic, Corros. Sci. 188 (2021) 109500. https://doi.org/10.1016/j.corsci.2021.109500.

[11] Wessman, Andrew, Laurence, Aude, Cormier, Jonathan, Villechaise, Patrick, Billot, Thomas, Franchet, Jean-Michel, Thermal Stability of Cast and Wrought Alloy Rene 65, Superalloys 2016, The Minerals, Metals & Materials Society, (2016) 793-800. https://doi.org/10.7449/Superalloys/2016/Superalloys_2016_793_800.

[12] R. Malacarne, S. Mathieu, L. Aranda, D. Diomande, C. Desgranges, S. Knittel, M. Vilasi, Type II hot corrosion of A718 and AD 730^{TM} polycrystalline Ni-based alloys: Influence of the SO_3 partial pressure, Corros. Sci. 224 (2023) 111550. https://doi.org/10.1016/j.corsci.2023.111550.

[13] C.S. Giggins, F.S. Pettit, Hot corrosion degradation of metals and alloys - a unified theory. Final scientific report, 1 June 1976-30 September 1978, Pratt and Whitney Aircraft, Middletown, CT (USA). Materials Engineering and Research Lab., 1979. https://doi.org/10.2172/5572795.

[14] F. Pettit, Hot Corrosion of Metals and Alloys, Oxid. Met. 76 (2011) 1–21. https://doi.org/10.1007/s11085-011-9254-6.

[15] B. Bordenet, High Temperature Corrosion in Gas Turbines: Thermodynamic Modelling and Experimental Results, Engineering, Materials Science, 106 (2004).

[16] M.A. DeCRESCENTE, N.S. Bornstein, Formation and Reactivity Thermodynamics of Sodium Sulfate With Gas Turbine Alloys, corrosion 24 (1968) 127–133. https://doi.org/10.5006/0010-9312-24.5.127.

[17] O. Morocutti, C. Duret-Thual, R. Morbioli, P. Steinmetz, Guide to the control of high temperature corrosion and protection of gas turbine materials, (1986). https://www.osti.gov/etdeweb/biblio/6231742 (accessed April 7, 2023).

[18] R. Rapp, Hot corrosion of materials: A fluxing mechanism?, Corros. Sci. 44 (2002) 209–221. https://doi.org/10.1016/S0010-938X(01)00057-9.

[19] E. Kistler, W.-T. Chen, G.H. Meier, B. Gleeson, A new solid-state mode of hot corrosion at temperatures below 700°C, Mater. Corros. 70 (2019) 1346–1359. https://doi.org/10.1002/maco.201810751.

[20] G. Dufour, D. Texier, T. Sanviemvongsak, T. Perez, S. Knittel, J. Bonnal, J. Ghanbaja, M. Emo, S. Migot, M. Vilasi, S. Mathieu, Type-II hot corrosion investigation of the DS200 +Hf superalloy at the γ/γ' scale, Corros. Sci. 255 (2025) 113095. https://doi.org/10.1016/j.corsci.2025.113095.

[21] R. Malacarne, S. Mathieu, M. Siblani, L. Aranda, S. Knittel, C. Desgranges, M. Vilasi, On the sulfation reaction of protective and transient oxides at 650 °C and its role in the low temperature hot corrosion mechanism, Corros. Sci. 218 (2023) 111186. https://doi.org/10.1016/j.corsci.2023.111186.

[22] A.K. Misra, D.P. Whittle, W.L. Worrell, Thermodynamics of Molten Sulfate Mixtures, J. Electrochem. Soc. 129 (1982) 1840. https://doi.org/10.1149/1.2124305.

[23] K.L. Luthra, D.A. Shores, Mechanism of Na2 SO 4 Induced Corrosion at 600°–900°C, J. Electrochem. Soc. 127 (1980) 2202. https://doi.org/10.1149/1.2129375.

[24] B.S. Lutz, J.M. Alvarado-Orozco, L. Garcia-Fresnillo, G.H. Meier, Na_2SO_4-Deposit-Induced Corrosion of Mo-Containing Alloys, Oxid. Met. 88 (2017) 599–620. https://doi.org/10.1007/s11085-017-9746-0.

[25] J.A. Goebel, F.S. Pettit, G.W. Goward, Mechanisms for the hot corrosion of nickel-base alloys, Metall. Trans. 4 (1973) 261–278. https://doi.org/10.1007/BF02649626.

[26] K.L. Luthra, Low Temperature Hot Corrosion of Cobalt-Base Alloys: Part II. Reaction Mechanism, Metall. Trans. A 13 (1982) 1853–1864. https://doi.org/10.1007/BF02647842.

[27] R.L. Jones, C.E. Williams, Mixed $MgSO_4$ - Na_2SO_4 Effects in the 973 K Hot Corrosion of CoCrAlY, J. Electrochem. Soc. 133 (1986) 217. https://doi.org/10.1149/1.2108527.

[28] E. Yazhenskikh, T. Jantzen, D. Kobertz, K. Hack, M. Müller, Critical thermodynamic evaluation of the binary sub-systems of the core sulphate system Na_2SO_4-K_2SO_4-$MgSO_4$-$CaSO_4$, Calphad 72 (2021) 102234. https://doi.org/10.1016/j.calphad.2020.102234.

[29] W.T. Wu, A. Rahmel, Inhibition of Hot Corrosion by $MgSO_4$ and $BaSO_4$ and its potential dependence, Mater. Corros. 35 (1984) 139–149. https://doi.org/10.1002/maco.19840350402.

[30] T. Gheno, M. Zahiri Azar, A.H. Heuer, B. Gleeson, Reaction morphologies developed by nickel aluminides in type II hot corrosion conditions: The effect of chromium, Corros. Sci. 101 (2015) 32–46. https://doi.org/10.1016/j.corsci.2015.08.029.

[31] L. Thébaud, Etude des relations entre microstructure et propriétés mécaniques du nouveau superalliage base nickel AD730, phdthesis, ISAE-ENSMA Ecole Nationale Supérieure de Mécanique et d'Aérotechique - Poitiers, 2017. https://theses.hal.science/tel-01735104 (accessed October 20, 2025).

[32] M.L. Hendery, M.T. Whittaker, B.J. Cockings, P.M. Mignanelli, The effect of salt composition on the stress-free and corrosion-fatigue performance of a fine-grained nickel-based superalloy, Corros. Sci. 198 (2022) 110113. https://doi.org/10.1016/j.corsci.2022.110113.

[33] D. Diomande, S. Mathieu, P.J. Panteix, M. Siblani, L. Aranda, C. Petitjean, M. Vilasi, Differential aeration corrosion of silver in sulfate melts at 900°C, Corros. Sci. 224 (2023) 111504. https://doi.org/10.1016/j.corsci.2023.111504.

[34] Barin I: Thermochemical Data of Pure Substances, Part I, VCH Verlags Gesellschaft, Weinheim, 1993.

[35] Knacke O., Kubaschewski O., Hesselman K., Thermochemical properties of inorganic substances, 2nd ed., Springer-Verlag, Berlin, pp.1-1113, (1991).

[36] S.K. Srivastava, B.N. Avasthi, Synthesis and characterization of indium intercalation compounds of tungsten disulphide: lnxWS_2 ($0 \leq x \leq 1$) Synth. Met. 10, 213-221 (1985).

[37] Glushko Thermocenter of the Russian Academy of Sciences, IVTAN Association, Izhorskaya 13/19, 127412 Moscow, Russia, 1994.

[38] C. Sha, L. Yang, J.M. Cairney, J. Zhang, D.J. Young, Sulphur diffusion through a growing chromia scale and effects of water vapour, Corros. Sci. 222 (2023) 111410. https://doi.org/10.1016/j.corsci.2023.111410.

[39] A.A. Bolzan, B.J. Kennedy, C.J. Howard, Neutron Powder Diffraction Study of Molybdenum and Tungsten Dioxides, Aust. J. Chem. 48 (1995) 1473–1477. https://doi.org/10.1071/ch9951473.